

Improving the Stability of Ambient Processed, SnO_2 -Based, Perovskite Solar Cells by the UV-Treatment of Sub-Cells

Gayathri Mathiazhagan, Aaron Seeber, Thomas Gengenbach, Simone Mastroianni, Doojin Vak, Anthony S. R. Chesman, Mei Gao, Dechan Angmo,* and Andreas Hinsch*

SnO_2 is nowadays the widely preferred material as an electron transport layer (ETL) in most n-i-p planar perovskite solar cells (PSCs) due to its facility for ambient, low temperature processing, and ultraviolet (UV) stability. Most reports published so far study device stability on full cells. Herein, the role of slot-die-coated SnO_2 on air-processed planar PSCs by analyzing sub-cells (indium tin oxide [ITO]/ SnO_2 /perovskite) under UV exposure is investigated. Results from UV-vis spectroscopy, depth profiling using X-ray diffraction measurement in grazing incidence mode (GIXRD), X-ray photoelectron spectroscopy (XPS), and photoluminescence spectroscopy measurements show that UV treatment of ITO/ SnO_2 /perovskite leads to a reduced electron transfer to the SnO_2 layer and a gradual increase in the amount of PbI_2 toward the perovskite surfaces. Subsequently, hole transport layer (HTL) and electrodes are applied on SnO_2 /perovskite interfaces (UV-treated and non-UV-treated) and complete devices are fabricated. Device performance is compared and analyzed through J - V curves and maximum power point (MPP) tracking. Results show that devices built on a UV-treated SnO_2 /perovskite interface show better stability attributed to the presence of excess PbI_2 resulting in a passivation effect. Challenges in uniform film formation of slot-die-coated SnO_2 and potential solutions using a polymeric additive are also highlighted.

with several commercial PV technologies on the market today.^[2] Commercializing PSCs requires not just an impressive PCE, but also capitalizing on their solution processability, and low-cost materials and production to achieve an unprecedented cost breakthrough. However, for the cost benefits of high-throughput production methods on plastic substrates such as polyethylene terephthalate to be realized, post-deposition thermal treatment steps are limited to 140 °C to avoid the degradation of the substrate.

In an n-i-p planar structure, the production of the electron transport layer (ETL) presents a critical challenge. Given its ubiquitous use in dye-sensitized solar cells (DSSCs), TiO_2 was the first widely used ETL, but the requirement of prolonged and high temperature (>450 °C) sintering made it incompatible with fast roll-to-roll manufacturing on low-cost substrates. In addition, the photocatalytic effect of TiO_2 has been reported to cause the degradation of the perovskite layer, particularly under ultraviolet (UV) light.^[3] These limitations


prompted the research into alternative low-cost metal oxide ETLs. Snaith and coworkers found the substitution of TiO_2 with Al_2O_3 greatly enhanced the stability of PSCs.^[3] Kelly and coworkers explored ZnO , a commonly used ETL in organic solar cells that could be processed at low temperature with environmentally benign solvents, such as water. However, ZnO proved to be

1. Introduction

Perovskite solar cells (PSCs) are becoming a highly competitive photovoltaic technology. Starting with a record power conversion efficiency (PCE) of 3.9% in 2009,^[1] PSCs have improved dramatically within a decade, with the current record of 25.2% at parity

G. Mathiazhagan, Dr. S. Mastroianni, Dr. A. Hinsch
Department of Organic and Perovskite Photovoltaics (OPP)
Division Photovoltaics
Fraunhofer Institute for Solar Energy Systems (ISE)
Heidenhofstrasse 2, 79110 Freiburg im Breisgau, Germany
E-mail: andreas.hinsch@ise.fraunhofer.de

Dr. A. Seeber, Dr. T. Gengenbach, Dr. D. Vak, Dr. A. S. R. Chesman,
Dr. M. Gao, Dr. D. Angmo
CSIRO Manufacturing
Flexible Electronics Laboratory
Research Way, Clayton VIC 3168, Melbourne, Australia
E-mail: dechan.angmo@csiro.au

 The ORCID identification number(s) for the author(s) of this article can be found under <https://doi.org/10.1002/solr.202000262>.

Dr. S. Mastroianni
Freiburg Materials Research Centre (FMF)
Albert Ludwigs University of Freiburg
George-Kohler allee 103, 79110 Freiburg im Breisgau, Germany

© 2020 The Authors. Published by WILEY-VCH Verlag GmbH & Co. KGaA, Weinheim. This is an open access article under the terms of the Creative Commons Attribution License, which permits use, distribution and reproduction in any medium, provided the original work is properly cited.

Correction added on 10 July 2020, after first online publication: Projekt Deal funding statement has been added.

DOI: 10.1002/solr.202000262

incompatible with PSCs; even though ZnO had a higher bulk electron mobility ($205\text{--}300\text{ cm}^2\text{ V}^{-1}\text{ s}^{-1}$) than TiO_2 , the presence of hydroxyl groups and acetate ligands quickly degraded the perovskite.^[4] Subsequent research examined ZnO ,^[4–6] ZnSO_4 ,^[7,8] WO_3 ,^[9,10] In_2O_3 ,^[11] SrTiO_3 ,^[12] and BaSnO_3 ,^[13,14] among others. However, none of these alternatives were as successful as SnO_2 . Due to its high mobility ($240\text{ cm}^2\text{ V}^{-1}\text{ s}^{-1}$), better energy-level alignment with perovskite, high transmittance, wider bandgap (-3.6 to -4.0 eV) with deep conduction and valence bands, and low-cost commercial availability, SnO_2 has emerged as the most promising ETL in planar PSCs with a highest certified efficiency of 23.32% PCE.^[15] With this achievement, it is increasingly important to rigorously test and understand the implications of SnO_2 on the stability of PSCs.

The stability of SnO_2 -containing devices has been studied under varied test conditions, such as dark storage,^[16–18] 1 sun illumination,^[19,20] and under UV exposure,^[19,21,22] however, conflicting conclusions have been drawn on the role of SnO_2 in perovskite degradation. This is partly due to the lack of standardized testing protocols and also because of the large differences in material and fabrication procedures. In certain tests, devices are stored in air or nitrogen environment^[23] and intermittent^[16,22,24] J – V measurements under standard 1 sun conditions (1000 W m^{-2} , AM 1.5G) were carried out. Such tests qualify as dark storage tests at room temperature (RT). Perovskite stability in dark storage tests is significantly higher compared with its operational stability under 1 sun test conditions, as the devices experience no long-term bias stress. For example, Chen et al. studied the stability of indium tin oxide (ITO)/ETL/CsFAMA/Spiro-OMeTAD/Au devices in which the ETL was either SnO_2 or graphite carbon nitride-doped SnO_2 ,^[25] with the devices processed in nitrogen. The devices with undoped SnO_2 retained over 80% of the initial PCE after 1000 h, which was significantly improved with doped SnO_2 .

In contrast to the dark storage test, a steady decline in PCE is reported when devices are subjected to constant 1 sun illumination, and the performance is monitored by intermittent J – V measurements or maximum power point (MPP) tracking.^[17,19,20] In other studies, UV tests are conducted and have shown varying results depending on the UV wavelength. For example, glass/ITO/ SnO_2 /MAPbI₃/Spiro-OMeTAD/Au devices showed negligible PCE degradation with UV-B (370 nm) irradiation over 1750 h, however, significant degradation occurred with UV-A (311 nm) exposure due to the degradation of the perovskite.^[21]

Instability due to the presence of SnO_2 has been attributed to mismatching energy-band levels leading to charge accumulation or localized crystallization-induced defects in SnO_2 from oxygen vacancies or, tin interstitial, and surface defects.^[25] Doping SnO_2 with Ga,^[23] EDTA,^[17] graphite carbon nitride SnO_2 ,^[25] or In_2O_3 ^[26] can alleviate the energy mismatch and reduce defects, leading to a slower rate of degradation. Nonetheless, all n-i-p devices show steady degradation regardless of the use of doped or undoped SnO_2 . The overall impact of SnO_2 cannot be easily discerned, as additional instability may also be attributed to the ubiquitously used hole transport material (HTM), Spiro-OMETAD.^[27–29] In addition, the use of an inert processing environment limits the implications of these studies in real-world devices, as maintaining an inert environment is costly and impractical in an industrial roll-to-roll manufacturing scenario.

Herein, we study the stability of devices incorporating SnO_2 produced by an industrially compatible slot-die coating method. We first examine the use of a slot-die-coated SnO_2 layer and device optimization as this coating technique presents several challenges to uniform film formation. We then present an investigation on the role of SnO_2 on the stability of ambient-processed PSC devices under UV irradiation. We study sub-cell configurations (glass/ITO/ SnO_2 /perovskite) before and after 500 h of UV (365 nm) irradiation under open circuit in a nitrogen-filled glovebox ($<1\text{ ppm H}_2\text{O}$, $<1\text{ ppm O}_2$). By doing so, we eliminate the effect of the hole transport layer (HTL) and electrode that typically fail first, which previously limited investigation into the role that other layers and interfaces play in device failure. We further compare results with TiO_2 and ZnO to discern the relative differences among the three metal oxides. Complete devices are built on the sub-cells (UV-treated and non-UV treated) and their performance and stability are analyzed. We show the importance of analyzing the sub-cell configurations to understand the specific interface kinetics, and also show that the stability of complete devices may not replicate the results from a sub-cell configuration. Unexpectedly, we find evidence that the SnO_2 /perovskite interface may not be stable under storage, however, UV irradiation can improve the interfacial stability.

2. Results and Discussion

2.1. Device Architecture

For the purpose of this study into SnO_2 /perovskite interface stability, PSCs with an n-i-p configuration were used. **Figure 1a** shows a schematic representation of the layers in the planar PSCs and the fabrication techniques used to produce them. The devices consist of prepatterned ITO-coated glass upon which SnO_2 was slot-die coated as the ETL, perovskite deposited via spin coating as the photoabsorber, and spin-coated anhydrous poly(3,4-ethylenedioxythiophene):polystyrene sulfonate (PEDOT:PSS) as the HTL. A thin interlayer of MoO_3 was vacuum evaporated on the HTL, and the devices were completed with a vacuum-deposited Ag counter electrode. The basic principle involved in this type of solar cell is that, upon AM 1.5G sun illumination, photogenerated charges are produced in the perovskite photoabsorber. The electrons are extracted by the ETL (SnO_2), whereas the holes are extracted by the HTL (PEDOT:PSS). The charges collected by the ETL pass through an external load and come back to the counter electrode to complete the circuit.

2.2. Fabrication and Characteristics of SnO_2 and Perovskite Films

An as-received nanoparticle solution of SnO_2 was slot-die coated on glass/ITO substrates. We observed that slot-die coating leads to the formation of SnO_2 agglomerates, even after 20 min of UV–ozone treatment of the substrate. SnO_2 agglomeration during film formation is undesirable for optimal device performance as the agglomerates can create shunt pathways in the device.^[24] This agglomeration occurs in slot-die films because it is a passive deposition process in which deposition and drying/evaporation are discrete sequential processes with the lag time between

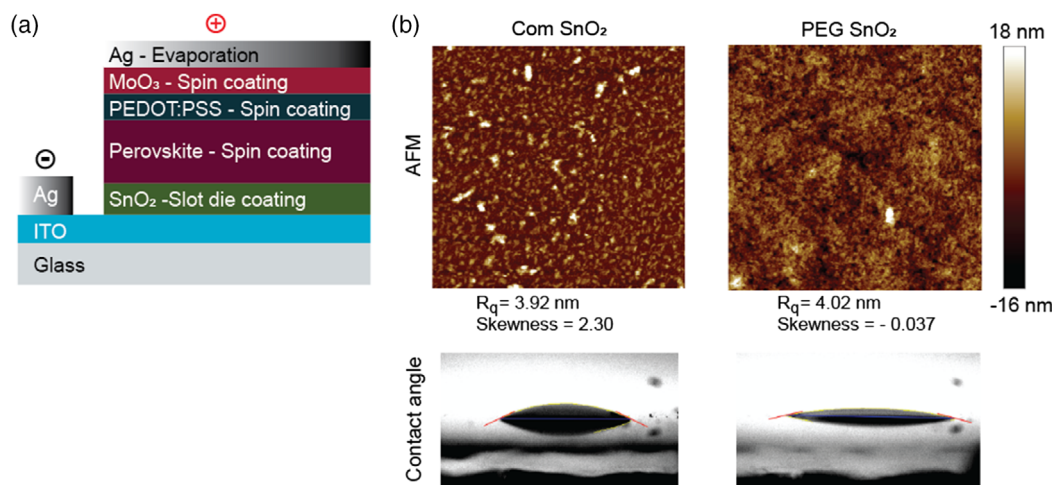


Figure 1. a) Schematic representation of an n-i-p planar PSCs together with its processing technique. b) AFM and CA measurements of as-brought SnO₂ (Com-SnO₂) and SnO₂ with PEG processed on ITO. The negative skewness factor and low CA for SnO₂ with PEG indicates the smooth layer morphology and the resultant improvement in layer wettability.

deposition and drying facilitating nanoparticles movement of nanoparticles leading to agglomeration. In contrast, such agglomerations are not observed in spin-coated films with UV treatment of the substrates, because spin coating is a dynamic process in which deposition and evaporation are concurrent mechanisms, leading to rapid drying of the film. In addition to the agglomeration challenge, perovskite precursors have poor wetting on the SnO₂ layer. As such, SnO₂ films are treated with UV-ozone prior to the deposition of perovskite precursor.^[30,31]

Surface modification through improved interface modification has been achieved by adding elements such as Li,^[32] Mg,^[33] Y,^[34] Sb,^[35] and Nb^[36] as dopants in SnO₂. To prevent agglomeration in the SnO₂ film and also to provide better wetting to the perovskite solution, we studied several additives, including polyethylene glycol (PEG), polyvinyl acetate (PVA), and ethylene glycol (EG). Among these, PEG addition gave the best film with slot-die coating, while also improving wettability of the perovskite solution. Figure 1b shows the atomic force microscopy (AFM) and contact angle (CA) measurement of SnO₂ layers with and without PEG, fabricated on an ITO-coated glass substrate. A clear difference in the layer morphology can be observed by comparing the AFM results. While roughness values are similar ≈ 4 nm, the PEG-SnO₂ layer has a negative skewness factor of -0.376 in comparison to the positive skewness of the commercial SnO₂ (com-SnO₂) films, the PEG-added SnO₂ film is uniform without any big particles or agglomerates. Figure S1, Supporting Information, shows the CA measurement for layers fabricated using SnO₂ with different additives; the lowest CA was measured for SnO₂ with PEG. This improved SnO₂ morphology is ascribed to the hydrogen bonding of PEG with SnO₂ which has improved the layer wettability.^[24] Thus, all the devices reported hereafter contain SnO₂ with PEG and referred to as SnO₂.

The morphology of the SnO₂ and perovskite layers was investigated using scanning electron microscope (SEM). Figure 2a,b shows the SEM images of slot-die-coated SnO₂ and the perovskite layer, respectively. Confirming the AFM results, no agglomeration of SnO₂ was observed, and a pinhole-free homogeneous

layer is shown in Figure 2a. The SEM image in Figure 2b shows the perovskite layer is conformally coated on the SnO₂ layer and is pin-hole free. As a comparison, an SEM image of a perovskite layer spin coated on glass is shown, as an inset in Figure 2b to show no difference to the perovskite layer when coated on SnO₂. Figure 2c,d shows the X-ray diffractograms of SnO₂ and perovskite, respectively. The diffractogram of SnO₂ shows that it has a tetragonal phase and belongs to the P42/mnm (136) space group. The absence of sharp peaks in the diffractogram indicates the slot-die-coated SnO₂ layer is nanocrystalline in nature. With the crystallite size calculated to be in the range of 2.5 ± 0.8 nm. Similar particle sizes of SnO₂ and its nanocrystallinity/amorphous property in the resultant layer for a solution-processed technique has also been observed in other reports.^[24,31,37] The result from X-ray diffraction (XRD) of a perovskite film is shown in Figure 2d. The peaks, shown in Figure 2d, correspond to cubic-phase perovskite (space group Pm-3m). A peak at 12.6° is also present, which corresponds to the (0 0 1) plane of PbI₂.^[38]

2.3. Device Performance

After optimization of the SnO₂ and perovskite layers, the devices are completed by depositing anhydrous PEDOT:PSS, onto which MoO₃ is evaporated to improve hole injection^[39,40] and in the end the counter electrode (Ag). The film thickness of SnO₂, perovskite, PEDOT:PSS, MoO₃, Ag were 70, 350, 80, 10, and 100 nm, respectively. The histogram of 133 complete devices is shown in Figure 3a to demonstrate the reproducibility of the devices reported in this article. The average electrical performances of these devices are V_{OC} of 920 mV, J_{SC} of 17.54 mA cm^{-2} , fill factor (FF) of 57.60%, and PCE of 9.32%. Figure 3b shows the $J-V$ curve of the champion device where V_{OC} of 960 mV, 18.34 mA cm^{-2} J_{SC} , 61.5% FF, and 10.82% PCE were achieved. Device performance is lower compared with literature values due to devices being fabricated under ambient

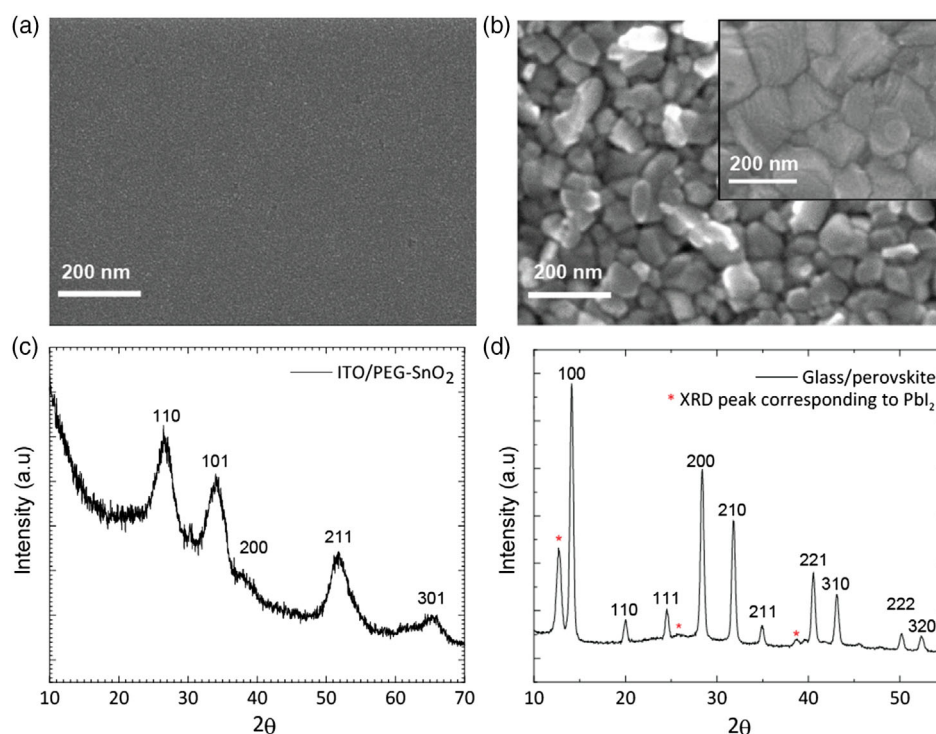


Figure 2. a) Top-view SEM image of slot-die-coated SnO_2 layer b) Top-view SEM image of spin-coated perovskite fabricated on SnO_2 . Inset shows the top-view SEM image of the perovskite layer on glass. c) XRD pattern of the SnO_2 layer. d) XRD pattern of the perovskite layer. SEM shows a homogeneous coating of SnO_2 and perovskite layers. In addition, the XRD shows that SnO_2 is nanocrystalline in nature and a cubic crystal phase for the perovskite has been presented.

conditions, as well as the non-optimal HTL.^[41,42] The PCE is, however, comparable with other reports on ambient-processed PSCs.^[43–48] Despite the lower PCE, we confirmed that the films were compact and that no shunt pathways (pin holes) were present by studying its V_{OC} under different light intensities (Figure 3c). The results show that all devices studied here retained V_{OC} at low sun intensity, confirming that the devices are shunt free. It is important to confirm this point as the presence of shunts accelerates the degradation and can interfere with the interpretation of results.^[49]

Figure 3d shows the energy-level diagram where a higher conduction band level of SnO_2 (−3.67 eV) was observed when compared with the values (−3.9 to −4.5 eV) shown most times in literature.^[17,19,25,32] This causes a mismatch at the SnO_2 /perovskite interface. It could have been caused by the slot-die coating of SnO_2 and requires further investigation beyond the current scope of this work. More information on the technique used to obtain the energy levels is provided in the Section 4.

2.4. Stability

2.4.1. Optical Characterization of Sub-cells Before and After UV Stress

Both internal and external factors contribute to a solar cell's instability. Light, heat, oxygen, and moisture are four-key external degradation factors. UV is the most prominent degradation-causing component in light due to its high energy. To study the effect

of UV light exposure, sub-cells comprising glass/ITO/ SnO_2 /perovskite photoelectrode was exposed to a UV lamp ($\lambda = 365$ nm with a power of 6 W emitted through two windows each comprising an area of 31.95 cm^2) placed at a distance of 21 cm for 500 h from the glass side leaving the perovskite layer openly exposed to the N_2 environment. **Figure 4a** shows the experimental setup. Using a sub-cell configuration, we eliminate any additional effects from the perovskite/HTL and HTL/electrode interfaces present in a complete cell and thereby avoid problems related to ion migration and incompatibility of the perovskite with the metal electrode are avoided.^[49] We carried out the tests inside a glovebox with oxygen and moisture levels of less than 1 ppm and at RT to eliminate competing degradation agents, as perovskite layers tend to rapidly degrade in the presence of oxygen and moisture.^[50–53] Ingress of moisture and oxygen can be avoided by the development of encapsulation in real-world applications. The sub-cells were characterized using photoluminescence (PL) spectroscopy and UV–vis spectroscopy before and after UV exposure.

Figure 4b shows light absorption spectra of sub-cells before and after 500 h of UV exposure. The light absorption through the 300–1000 nm range decreased slightly for UV-treated sub-cells in comparison with non-UV-treated fresh sub-cells, which indicates degradation upon UV irradiation.^[54,55] This could arise due to degradation within the perovskite or the perovskite/ SnO_2 interface, or a combination of both. We probed degradation within the perovskite layer by studying glass/perovskite films under similar experimental conditions. Figure 4c shows the light absorption spectra of glass/perovskite films before and after

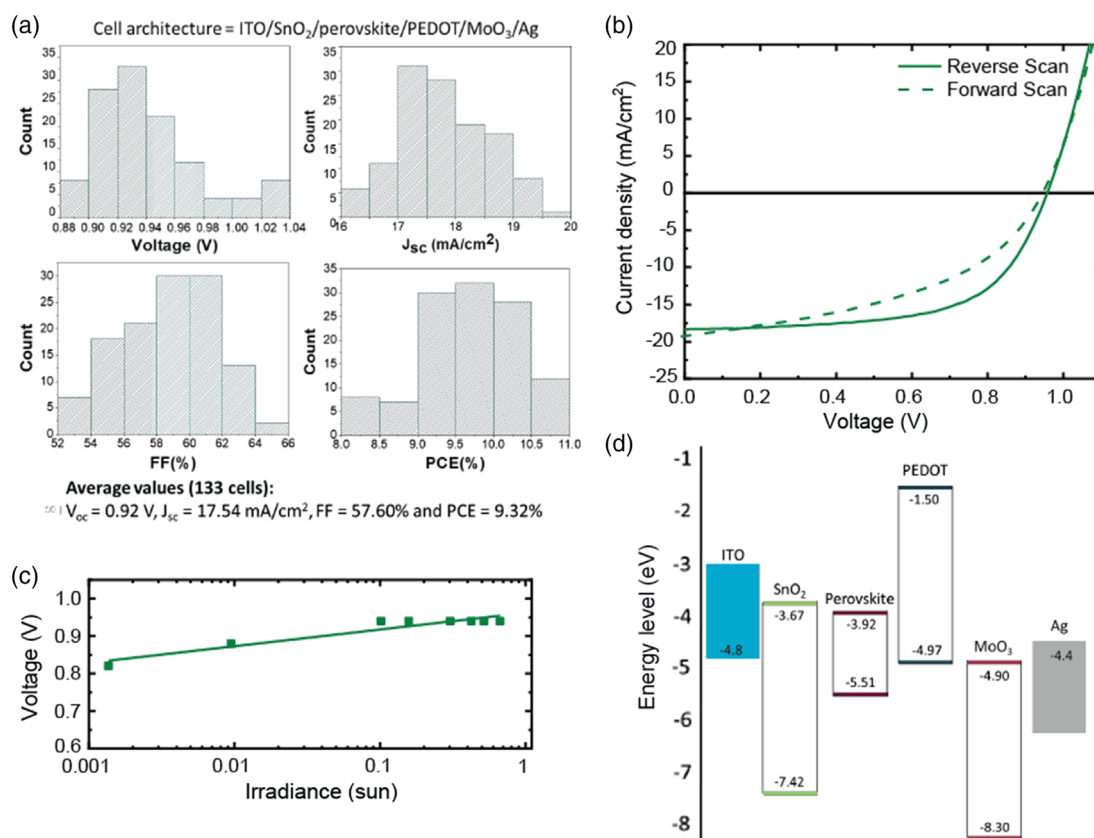


Figure 3. a) Histogram of electrical performances of 133 devices with architecture ITO/SnO₂/perovskite/PEDOT/MoO₃/Ag. Their average electrical parameters have also been calculated to show the reproducibility of the devices. b) J–V curve of the champion device presenting a PCE of 10.82% whose active area was 0.1 cm² measured under AM 1.5G at a scan rate of 100 mV s^{−1}. c) Suns–V_{oc} measurement and d) energy band diagram. Shunt-free reproducible devices have been demonstrated for further stability analysis.

500 h of UV treatment, and of glass/perovskite film before and after 500 h of storage in the same glovebox but without any UV treatment. The spectra reveal absorption has decreased to a similar extent in both the stored and the UV-treated sample, which suggest perovskite degrades and UV treatment does not exacerbate or alleviate the rate of degradation of the perovskite film itself. However, the decrease in absorption of the sub-cells shown in Figure 4b is comparatively lower than the decrease in absorption of perovskite only films in Figure 4c, which indicate that UV treatment of sub-cells may indeed reduce the degradation of perovskite.

Figure 4d shows the PL measurement of a freshly prepared sub-cell and a UV-treated sub-cell. The PL intensity significantly increased after UV exposure, which suggests a reduced electron transfer from the photogenerated electron–hole pair of the perovskite to the SnO₂ layer when compared with samples without UV exposure. The reduced electron transfer, therefore, indicates changes at the SnO₂/perovskite interface or of the bulk perovskite after the UV exposure. To find out whether the degradation is due to the bulk perovskite or due to its interface with SnO₂, we exposed a glass/perovskite film to UV light for 500 h to probe the bulk perovskite as a reference. The PL spectra of glass/perovskite films with and without UV treatment are shown in Figure 4e. UV treatment of the glass/perovskite indeed

decreased the PL intensity, indicating that the perovskite itself degraded under the UV light, in accordance with UV–vis results. This might be because of the longer lived electron–hole pair charges are not extracted because of the absence of electrode which can lead to adverse side reactions.^[15,56,57]

To further attest whether the presence of SnO₂ can alleviate the degradation of the perovskite, we compared the PL before and after UV exposure of glass/ITO/SnO₂/perovskite with other metal oxides, such as ZnO and TiO₂. Figure S2, Supporting Information, shows that the PL peak intensity of both glass/ITO/SnO₂/perovskite and glass/ITO/TiO₂/perovskite increased after 48 h of UV exposure, whereas the peak PL intensity of ZnO/perovskite decreased significantly after UV exposure, which suggests that the perovskite has degraded significantly in the presence of ZnO. It is also known that the TiO₂/perovskite interface is adversely affected in the presence of UV^[3] which caused the reduced charge-transfer efficiency upon UV irradiation. Nevertheless, SnO₂ shows similar trend as TiO₂.

2.4.2. GIXRD Analysis on Sub-cells Before and After UV Stress

Figure 5a shows grazing incidence X-ray diffractograms taken at 0.25° to study the influence of UV at the surface.

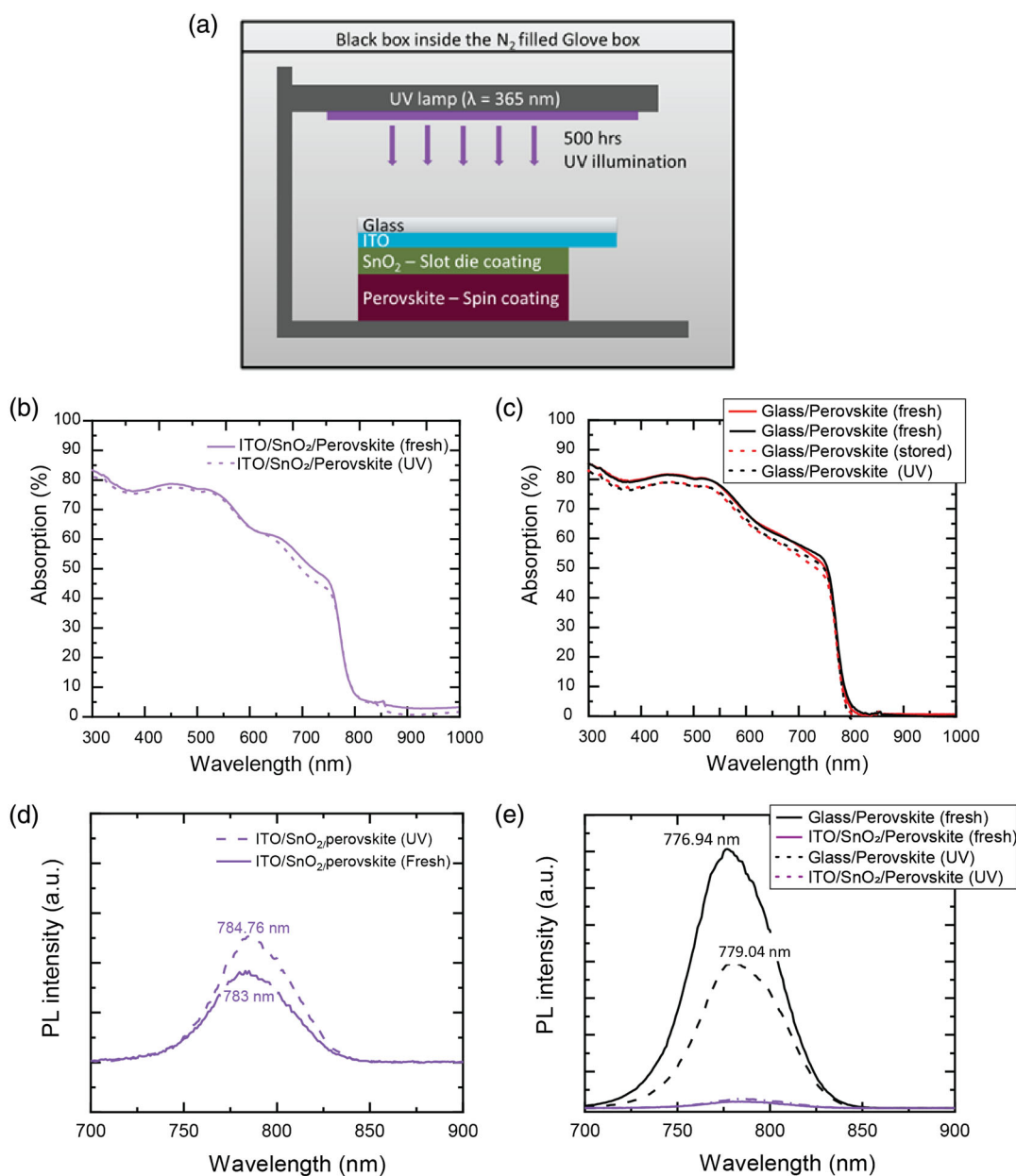


Figure 4. a) Schematic representation of the experimental setup for UV stress for 500 h inside a glovebox where sub-cells (glass/ITO/ SnO_2 /perovskite) were illuminated from the glass side using a UV lamp of 365 nm with 6 W lamp power source. b) UV-vis spectrum of a glass/ITO/ SnO_2 /perovskite sub-cell before and after UV stress for 500 h. c) UV-vis spectrum of glass/perovskite films before and after UV stress of 500 h and before and after storage in the glovebox without UV for 500 h. d) PL spectrum of a glass/ITO/ SnO_2 /perovskite sub-cells before and after UV stress for 500 h and e) PL spectroscopy results of a glass/perovskite before and after UV stress for 500 h. Decrease in PL in glass/perovskite and increase in PL in glass/ITO/ SnO_2 /perovskite sub-cell after 500 h UV exposure shows that perovskite quality has degraded, and there is also a poor transfer of electrons from perovskite to SnO_2 at the SnO_2 /perovskite interface.

Glass/ITO/ ZnO /perovskite film shows the highest evolution of PbI_2 phase as evident in the peak at $2\theta = 12.6^\circ$ which corresponds to PbI_2 (0 0 1) phase. The relative peak intensities of the PbI_2 (0 0 1) phase with respect to the perovskite (1 0 0) phase are similar for both glass/ITO/ SnO_2 /perovskite and glass/perovskite indicating that SnO_2 does not increase the degradation of perovskite at the surface.

To probe deeper into the bulk of the perovskite and the SnO_2 /perovskite interface, XRD was carried out in grazing incidence mode (GIXRD) at several incidence angles ranging from 0.25° to 1.3° for glass/ITO/ SnO_2 /perovskite sub-cells before and after 500 h UV stress. The results were further compared with glass/ITO/ ZnO /perovskite and glass/perovskite. The low incidence angle grazes the surface while higher angles

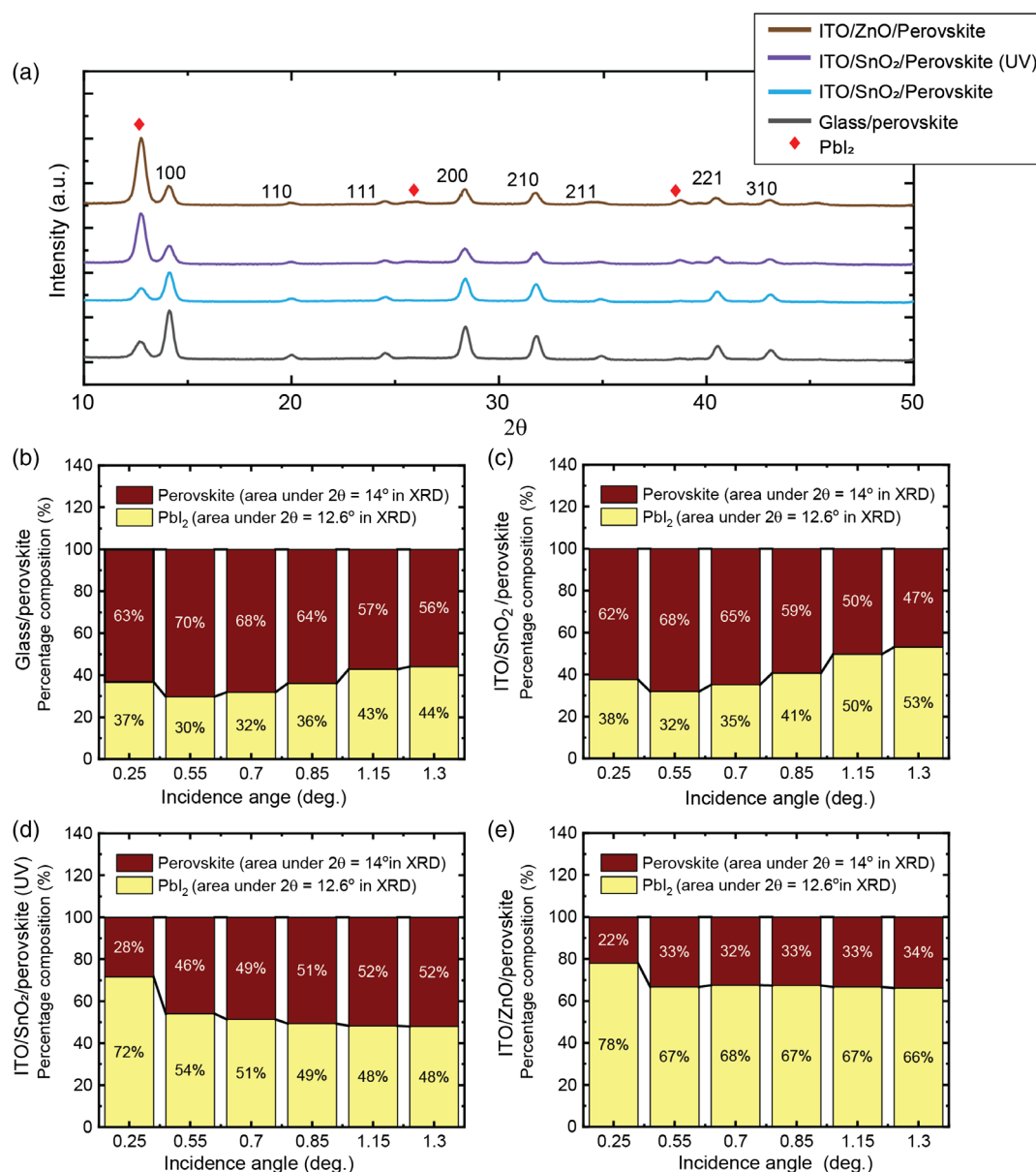


Figure 5. a) GIXRD diffractograms taken at an incidence angle of 0.25° of freshly prepared glass/ITO/ZnO/perovskite, glass/ITO/SnO₂/perovskite, and glass/perovskite compared with glass/ITO/SnO₂/perovskite—UV stressed for 500 h. Percentage composition of the area under the curve of $2\theta = 12.6^\circ$ (for PbI₂ phase 0 0 1) and $2\theta = 14^\circ$ (for perovskite phase 1 0 0) for various GIXRD incidence angles for b) glass/perovskite, c) glass/ITO/SnO₂/perovskite, d) glass/ITO/SnO₂/perovskite—UV stressed for 500 h, and e) glass/ITO/ZnO/perovskite.

probe into the bulk perovskite towards the ETL/perovskite interface.

The bar graphs in Figure 5b–e show the phase composition of PbI₂ and perovskite seen in the four samples at various GIXRD incidence angles by plotting the relative ratio of the integrated peak intensity for the (0 0 1) PbI₂ peak located at 12.6° with respect to the integrated intensity of the main perovskite (1 0 0) peak at 14°. The comparison of glass/perovskite and glass/ITO/SnO₂/perovskite reveals similar results (37% and 38% of PbI₂, respectively) at the surface. However, the relative proportion of PbI₂ increases in the glass/ITO/SnO₂/perovskite sample as one

probes deeper into the bulk toward the interface in comparison with glass/perovskite films, indicating the possibility of enhanced interfacial degradation due to the presence of SnO₂ (Figure 5b,c).

Comparing the UV-treated and non-UV-treated sub-cells, it is observed that a relatively higher proportion of PbI₂ (72%) is present at the surface of the UV-treated sub-cell, as shown in Figure 5d. This could be induced by photo-oxidative reaction at the perovskite surface with residual oxygen and water which may be present in the glovebox, leading to a loss of iodine. A similar observation has been reported by Ouyang et al.^[58,59]

In the case of the glass/ITO/ZnO/perovskite configuration (Figure 5e), a high proportion of PbI_2 (78%) at the surface has been observed with a uniform PbI_2 amount being present throughout the bulk of the film. The PL also shows that there is a much faster degradation of the perovskite occurring in the presence of ZnO as the reaction can be observed in a few minutes when ZnO is deposited under ambient atmospheric conditions. The degrading effect of ZnO on the perovskite has been attributed to photocatalytic reactions^[60] due to the presence of hydroxyl groups. Thus, our results show that the degradation of perovskite in the presence of SnO_2 is much less pronounced.

2.5. MPP Tracking of Complete Devices

To investigate the effect of UV treatment on the operational stability of planar n-i-p PSCs, we completed the cells by depositing PEDOT:PSS as the HTL, MoO_x , and Ag on top of the UV-treated (500 h) glass/ITO/ SnO_2 /perovskite. MoO_x was used to create a barrier against Ag and I reacting, which can lead to degradation of the contact.^[49] For comparison, the devices were also fabricated on the non-UV-treated glass/ITO/ SnO_2 /perovskite sub-cell with PEDOT:PSS, MoO_x , and Ag. Hereafter, for simplification, glass/ITO/ SnO_2 /perovskite is referred to as the sub-cell.

Figure 6a shows the normalized MPP of devices made from a UV-treated sub-cell and a non-UV-treated sub-cell after 500 h of full-cell fabrication, acquired for 14 h under continuous 1 sun illumination in a N_2 -filled glovebox. The MPP tracking of a device made from non-UV-treated sub-cell starts to show constant linear decay 5 days after fabrication (Figure S3, Supporting Information).

In contrast, the MPP of the device made from a UV-treated sub-cell shows an abrupt initial decay with a loss of only 20% of initial MPP value within 3–4 h followed by a stabilized trend. The degradation is similar to that observed in organic solar cell devices where the initial rapid degradation is known as the “burn-in.”^[61] As shown for MAPbI_3 films,^[57,59,62–64] oxygen can substantially be trapped inside the perovskite, which might lead to a similar effect in the initial stability.

As the sub-cells were fabricated in ambient condition, the surface of the films and the grain boundaries are likely to contain a higher concentration of adsorbed oxygen and moisture, which triggers degradation upon UV illumination.^[50] This is evident in the XRD depth profiling which revealed an higher relative presence of PbI_2 on the film surface of the UV-treated sub-cell compared with the non-UV-treated sub-cell (Figure 5c,d). X-ray photoelectron spectroscopy (XPS) depth profiling also indicates a gradient of PbI_2 concentration for the UV-treated sub-cells. A full discussion of the XPS results is given in Figure S4, Tables S1 and S2, Supporting Information. This accumulation of additional PbI_2 at the perovskite/electrode interfaces will induce a passivation effect by reduction of defect states,^[65] ion defect migrations,^[66] and recombination sites^[54,67] which would lead to the stabilization of MPP in the devices made of UV-treated sub-cells.

Figure 6b,c shows the comparison between the normalized photovoltaic parameters acquired from the J - V curves before and after the MPP measurement. Their corresponding J - V curves are provided in Figure S5, Supporting Information. The devices with a non-UV-treated sub-cell undergo a linear

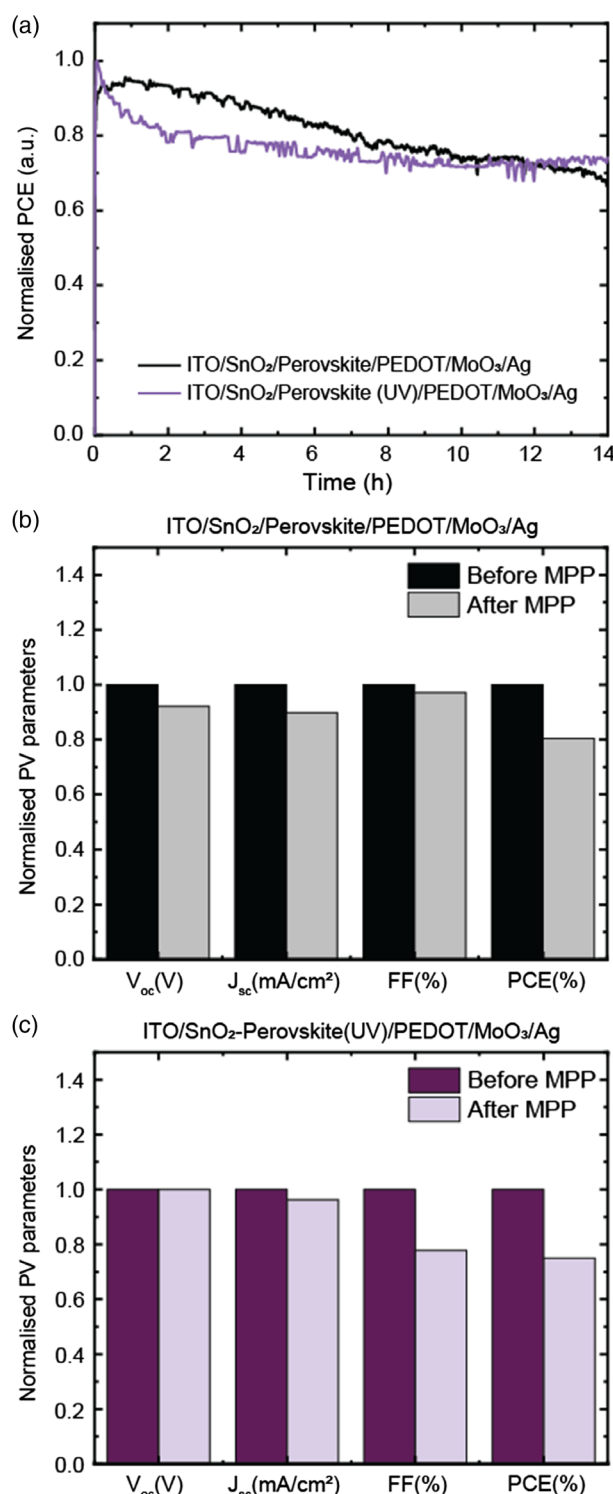


Figure 6. a) Comparison of normalized MPP of devices whose glass/ITO/ SnO_2 /perovskite interface is UV treated with devices whose glass/ITO/ SnO_2 /perovskite interface is not UV treated. Comparison of normalized electrical parameters taken from J - V curves acquired before and after MPP for b) devices made from non-UV-treated sub-cells and c) devices made from UV-treated sub-cells. A linear decay trend is observed in devices made of non-UV-treated sub-cell, whereas the MPP stabilized after 4 h for devices made of UV-treated sub-cell.

reduction in all photovoltaic parameters, particularly V_{OC} and J_{SC} , which suggests degradation in bulk and interfaces, whereas, devices with UV-treated sub-cells have similar J_{SC} and V_{OC} with somewhat reduced FF, which could be due to contact issues triggered by a high concentration of PbI_2 on the surface. Detailed information on the reproducibility of the devices is shown in Figure S6, Supporting Information.

3. Conclusions

In this article, we investigated the effect of slot-die-coated SnO_2 on the UV stability of perovskite films. We demonstrate the challenges of forming a uniform film with slot-die coating SnO_2 and solved the problem of agglomeration by adding PEG as a polymeric additive. We characterized the formed SnO_2 ETL using XRD and found that the layer is nanocrystalline in nature. In comparison with the literature, we observed a significant positive shift in the range of 0.2–0.8 eV in the conduction band level of SnO_2 (−3.67 eV) using UPS which might originate from film formation differences owing to slower solvent evaporation in a slot-die coating process compared with the often-used spin coating.

To particularly investigate the SnO_2 /perovskite interface's contribution to device stability, we characterized the glass/ITO/ SnO_2 /perovskite sub-cells before and after 500 h continuous UV illumination under N_2 environment from the glass side. We also investigate perovskite films on glass alone as control samples to rule out the influence of bulk degradation. Absorption spectra of all perovskite films and sub-cells showed little change after UV treatment. However, higher PL intensity was observed after the UV treatment in sub-cells, which indicated a lower electron injection efficiency into the electron-accepting SnO_2 layer. In addition, GIXRD measurements show the presence of excess PbI_2 which are formed at the surfaces of perovskite photoabsorber after the UV treatment. XPS measurements also confirmed the observations of GIXRD. Subsequently, devices were completed from sub-cells to full devices through a HTL and electrode deposition. During the MPP tracking, unlike the constant drop of PCE observed in the case of the device with non-UV-treated sub-cell, 80% of the initial PCE was retained for 10 h after the initial decrease in a device with UV-treated sub-cell. This is attributed to the passivation effect from the presence of excess PbI_2 at the HTL/perovskite interface.

In conclusion, detrimental effects have been noticed in the sub-cells after long UV illumination. However, surprisingly, complete devices fabricated from UV-treated sub-cells showed stable performance. Therefore, to understand further the device stability under UV, we show the importance of analyzing also a specific interface in a sub-cell. Analyzing a sub-cell can therefore be a powerful tool to probe layers and interfaces across a plethora of characterization tools. While UV treatment of sub-cells shows unexpected improvement in the full device stability, future work should explore stability over different duration and the impact of HTLs other than PEDOT:PSS. In addition, this study indicates that UV treatment of sub-cells may be an effective passivation tool. For this, various parameters including UV intensity, wavelength, and duration of exposure requires further investigation.

4. Experimental Section

Chemicals: PbI_2 (99.99%) and $PbCl_2$ (99.99%) were sourced from TCI Chemicals. MAI and FAI were sourced from GreatCell Solar. CsI (>99%), Description dimethylformamide (DMF), dimethyl sulfoxide (DMSO), ethyl acetate were sourced from Sigma-Aldrich. All solvents were anhydrous grade. All chemicals were used as received. PEDOT:PSS (Clevios SEJ 272, pH neutralized anhydrous formula in anisole) was sourced from Hereaus.

Precursor Solution Preparation: The SnO_2 solution was prepared by the procedure defined by Wei et al.^[24] About 225 μ L of SnO_2 solution (2.25 mL of Sn_2O 15% in H_2O colloidal dispersion liquid from Alfa Aesar dissolved in 10 mL DI water) was added to 1.5 mL of $LiCl_2$ solution (17 mg/4 mL DI water). The mixture is stirred for 10 min @ RT and 5 mg of PEG (from Sigma-Aldrich with molecular weight 8000 K) was added and stirred overnight.

About 1 M of $MAPbI_3$, $FAPbI_3$, and $MAPbBr_3$ using DMF (as solvent was prepared. In addition, 0.85 M of $CsPbI_3$ in DMF:DMSO (4:1 v/v) was also prepared. The precursor solutions were prepared in a glovebox and stirred at 70 °C overnight. For the final CsMAFA solution, $MA_{0.61}FA_{0.37}Cs_{0.02}PbI_{2.96}Br_{0.074}$ was mixed with 2.5 mol% of $PbCl_2$ together with 10 ppm of L- α -phosphatidylcholine (Sigma-Aldrich) as a surfactant. The recipe was optimized from previously reported by Tang et al.^[68] This solution was further stirred at 70 °C for 2 h.

Device Fabrication: Prepatterned ITO-coated glass substrates (Shenzhen Display, 5 Ω sq^{−1}) were used for the fabrication of devices. The substrates were sequentially cleaned in an ultrasonic bath using a detergent solution (5 vol% Deconex 12 PA), twice with deionized water, acetone, and propan-2-ol for 5 min each, with drying under a nitrogen stream between each step. The substrates were UV-ozone-treated using Novascan PDS-UVT for 20 min prior to slot-die coating the SnO_2 .

The SnO_2 solution was slot-die coated with a bed temperature of 50 °C and a coating speed of 10 mm s^{−1}. The samples were annealed for 20 min at 200 °C, resulting in a 70 nm thick SnO_2 layer. About 100 μ L of the perovskite solution was spin coated with two-step spin speed of 2000 RPM for 5 s and 3500 RPM for 35 s. About 500 μ L of ethyl acetate as antisolvent was deposited onto the surface of the perovskite 7 s after the start of second spin speed setting. Samples were then annealed at 100 °C for 2 min resulting in a 350 nm-thick perovskite layer. About 75 μ L of the PEDOT:PSS was spin coated at 5000 RPM for 30 s to give an 80 nm HTL layer. All the solution-based deposition until HTL layer is carried out in air under ambient conditions.

Samples were then transported to an evaporator (Angstrom) in a glovebox to evaporate 10 nm MoO_3 as an interlayer and 100 nm of Ag (99.9% pure, Kurt J. Lesker Company) or Au as counter electrode. About 10^{−7} Torr vacuum condition was used. The active area of the devices was defined as 0.1 cm² using an evaporation mask and cross-checked with laser-beam-induced imaging.

Device Measurements: The J – V curves were measured under an inert atmosphere using a Keithley 2400 Source Meter under standard solar irradiation (AM 1.5G, 100 mW cm^{−2}). The light intensity was calibrated using a reference cell (Hamamatsu S1133 with KG5 filter, 2.8 × 2.4 mm of photosensitive area), which was calibrated by a certified reference cell (PV Measurements, certified by NREL) under 1000 W m^{−2} AM 1.5G illumination from an Oriel AAA solar simulator fitted with a 1000 W Xe lamp. The reverse scan was measured from 1.0 to −0.1 V and vice versa for the forward scan where the scan rate was fixed to be 100 mV s^{−1}. The cell area of 0.1 cm² was defined by shadow mask area used the Ag evaporation. MPP was measured under the same solar simulator. For low intensity measurements, the sun intensity was controlled using optical filters from Newport with different optical densities. Its corresponding percentage of transmittance varied from 100% to 0.01%. For UV exposure, a hand-held model of UV lamp (UVL-56) from UVP, USA was used. The wavelength of the UV light was 365 nm, and output power were 6 W. The source was emitted through two windows each with an area of 31.95 cm². The samples were placed at a distance of 21 cm from the UV source. Photovoltaic measurements and UV exposure were conducted inside the glovebox.

SEM images were taken using Zeiss Merlin field emission microscope using electron gun voltage of 5 kV and working distance between 5 and 6 mm. Images were captured using InLens detector. CA measurements

were carried out using instrument by Nanotechnology Instruments. CA was measured with perovskite solution.

A Bruker FastScan atomic force microscope with Icon scanning head and NanoScope 9.4 software was used to measure surface topography. Ultrasharp silicon nitride tips were used to image under ambient conditions. The tips have a typical force constant of 0.4 N m^{-1} and a resonant frequency of 70 kHz. Scan size of $2 \mu\text{m}$ were carried out at 0.7 Hz and 512 data points per scan line. All images were processed and linescans obtained using NanoScope Analysis 1.9 software.

The PL spectra were measured using the fluorescence spectrophotometer from Perkin Elmer (model no. LS55). The excitation wavelength was set as 520 nm with slit width of 5 for emission and excitation. A UV-vis spectrophotometer from Hewlett-Packard/Agilent 8453 equipped with an integrated sphere was used to accurately measure transmission and reflection, from which absorption was calculated. Photoelectron spectroscopy in air (PESA) measurements were carried out using a Riken Keiki AC-2 spectrometer to obtain the ionization potential of perovskite and PEDOT:PSS. For all samples, a power intensity of 20 nW was used. The data were plotted as energy versus the square root of the electron count, as defined by a power number of 0.5.

A Rigaku SmartLab with a rotating anode Cu K α source (45 kV, 200 mA), equipped with a Hypix 3000 detector was used to obtain grazing incidence XRD patterns. The diffractometer was configured with 0.079–0.176 mm incidence slits and a beam limiting mask of 10 mm. The samples were set atop a Si zero background plate to ensure no contribution from the sample stage. Data were collected over the 2θ range 10° – 115° with a step size of 0.04° and a step rate of 2° per minute. Analysis was carried out on the collected XRD data using the Bruker XRD search match program EVA5. Crystalline phases were identified using the ICDD-JCPDS powder diffraction database. Perovskite matched with PDF# 01-085-6374, PbI $_2$ with PDF# 04-009-6453, and SnO $_2$ with PDF# 04-014-0193. Pawley analyses were carried out on the data using the Bruker TOPAS V5 program for lattice parameter calculations. Background signal was described using a combination of Chebyshev polynomial linear interpolation function and $1/x$ function. Cell parameters, vertical sample displacement, peak full width at half maximum, and peak scale factors were all refined. Error ranges were calculated on the basis of three estimated standard deviations as calculated by TOPAS.

XPS analysis was conducted using an AXIS Nova spectrometer (Kratos Analytical Inc., Manchester, UK) with a monochromated Al K α source at a power of 180 W (15 kV \times 12 mA), a hemispherical analyzer operating in the fixed analyzer transmission mode and the standard aperture (analysis area: $0.3 \times 0.7 \text{ mm}^2$). The total pressure in the main vacuum chamber during analysis was typically between 10^{-9} and 10^{-8} mbar. Survey (wide scan) spectra were acquired at a pass energy of 160 eV. Each specimen was analyzed at an emission angle of 0° as measured from the surface normal. Assuming typical values for the electron attenuation length of relevant photoelectrons the XPS analysis depth (from which 95% of the detected signal originates) ranges between 5 and 10 nm for a flat surface. Depth profiling experiments were conducted using an Ar Gas Cluster Ion Source (GCIS; Kratos Analytical Inc. Minibeam 6) operated at a cluster size of Ar1000+ with an impact energy of 10 keV, equating to a partition energy of 10 eV per atom. For the ion beam, a raster size of 2 mm^2 (1.4×1.4) was used. A stable beam current was confirmed prior to performing the depth profile experiment by measuring the sample current on the earthed sample platen (between 10 and 20 nA). Data processing was carried out using CasaXPS processing software version 2.3.15 (Casa Software Ltd., Teignmouth, UK). All elements present were identified from survey spectra. The atomic concentrations of the detected elements were calculated using integral peak intensities and the sensitivity factors supplied by the manufacturer. The accuracy associated with quantitative XPS is ≈ 10 –15%. Precision (i.e., reproducibility) depended on the signal/noise ratio but is usually much better than 5%. The latter is relevant when comparing similar samples.

Ultraviolet photoelectron spectroscopy (UPS) analysis was used to obtain the ionization potential of SnO $_2$. It was conducted using an AXIS Nova spectrometer (Kratos Analytical Inc., Manchester, UK) with a He discharge UV lamp using He I radiation (incident photoenergy:

21.22 eV), a hemispherical analyzer operating in the fixed analyzer transmission mode and the standard aperture (analysis area: $0.3 \times 0.7 \text{ mm}^2$). The samples were biased at -9 V to facilitate the observation of the secondary electron cutoff from the UPS spectra. The total pressure in the main vacuum chamber during analysis was typically 10^{-8} mbar. Spectra were acquired at a pass energy of 5 eV with a step width of 0.025 eV.

The work function was calculated from the secondary electron cutoff (E_{cutoff}) measured from the UPS spectra and the incident photo energy using the following equation

$$\text{Work function} = 21.22 - E_{\text{cut off}} \quad (1)$$

The ionization potential (I_p) was determined from the onset of the HOMO ($\text{HOMO}_{\text{onset}}$) using the following equation

$$I_p = 21.22 - (E_{\text{cut off}} - \text{HOMO}_{\text{onset}}) \quad (2)$$

Supporting Information

Supporting Information is available from the Wiley Online Library or from the author.

Acknowledgements

The authors thank CSIRO Materials Characterization Program, especially Mark Greaves, Melisja De Vries, Taehyo Kim and Chris Easton. G.M. acknowledges the scholarship support by the State Graduate Funding Program of Baden-Württemberg (LGFG), Germany. D.A., D.V., and M.G. acknowledge support from Australian Centre of Advanced Photovoltaics (ACAP) and Australian Renewable Energy Agency (ARENA) (grant agreement 2017/RND012). S.M. and A.H. gratefully acknowledges the funding by the Project PROPER financed from the German Federal Ministry of Education and Research under the funding no. 01DR19007. The authors acknowledge the project UNIQUE, supported under the umbrella of SOLAR-ERA.NET_Cofund by ANR, PtJ, MIUR, MINECOAEI, SWEA. SOLAR-ERA.NET supported by the European Commission within the EU Framework Programme for Research and Innovation HORIZON 2020 (Cofund ERANET Action, no. 691664). This publication reflects only the author's views and the European Union is not liable for any use that may be made of the information contained therein. Open access funding enabled and organized by Projekt DEAL.

Conflict of Interest

The authors declare no conflict of interest.

Keywords

planar perovskites, slot-die coating, SnO $_2$, sub-cells, UV stability

Received: May 25, 2020

Revised: June 17, 2020

Published online:

- [1] A. Kojima, K. Teshima, Y. Shirai, T. Miyasaka, *J. Am. Chem. Soc.* **2009**, *131*, 6050.
- [2] NREL, <https://www.nrel.gov/pv/cell-efficiency.html> (accessed: May 2020).
- [3] T. Leijtens, G. E. Eperon, S. Pathak, A. Abate, M. M. Lee, H. J. Snaith, *Nat. Commun.* **2013**, *4*, 2885.
- [4] J. Yang, B. D. Siempelkamp, E. Mosconi, F. de Angelis, T. L. Kelly, *Chem. Mater.* **2015**, *27*, 4229.

- [5] D.-Y. Son, J.-H. Im, H.-S. Kim, N.-G. Park, *J. Phys. Chem. C* **2014**, 118, 16567.
- [6] J. Kim, G. Kim, T. K. Kim, S. Kwon, H. Back, J. Lee, S. H. Lee, H. Kang, K. Lee, *J. Mater. Chem. A* **2014**, 2, 17291.
- [7] E. J. Yeom, S. S. Shin, W. S. Yang, S. J. Lee, W. Yin, D. Kim, J. H. Noh, T. K. Ahn, S. I. Seok, *J. Mater. Chem. A* **2017**, 5, 79.
- [8] A. Bera, A. D. Sheikh, M. A. Haque, R. Bose, E. Alarousu, O. F. Mohammed, T. Wu, *ACS Appl. Mater. Interfaces* **2015**, 7, 28404.
- [9] K. Wang, Y. Shi, Q. Dong, Y. Li, S. Wang, X. Yu, M. Wu, T. Ma, *J. Phys. Chem. Lett.* **2015**, 6, 755.
- [10] J. Zhang, C. Shi, J. Chen, Y. Wang, M. Li, *J. Solid State Chem.* **2016**, 238, 223.
- [11] M. Qin, J. Ma, W. Ke, P. Qin, H. Lei, H. Tao, X. Zheng, L. Xiong, Q. Liu, Z. Chen, J. Lu, G. Yang, G. Fang, *ACS Appl. Mater. Interfaces* **2016**, 8, 8460.
- [12] A. Bera, K. Wu, A. Sheikh, E. Alarousu, O. F. Mohammed, T. Wu, *J. Phys. Chem. C* **2014**, 118, 28494.
- [13] S. S. Shin, E. J. Yeom, W. S. Yang, S. Hur, M. G. Kim, J. Im, J. Seo, J. H. Noh, S. I. Seok, *Science* **2017**, 356, 167.
- [14] L. Zhu, Z. Shao, J. Ye, X. Zhang, X. Pan, S. Dai, *Chem. Commun.* **2016**, 52, 970.
- [15] Q. Jiang, Y. Zhao, X. Zhang, X. Yang, Y. Chen, Z. Chu, Q. Ye, X. Li, Z. Yin, J. You, *Nat. Photonics* **2019**, 13, 460.
- [16] Y. Zhao, J. Wei, H. Li, Y. Yan, W. Zhou, D. Yu, Q. Zhao, *Nat. Commun.* **2016**, 7, 10228.
- [17] D. Yang, R. Yang, K. Wang, C. Wu, X. Zhu, J. Feng, X. Ren, G. Fang, S. Priya, S. F. Liu, *Nat. Commun.* **2018**, 9, 3239.
- [18] A. J. Yun, J. Kim, T. Hwang, B. Park, *ACS Appl. Energy Mater.* **2019**, 2, 3554.
- [19] S. Wang, Y. Zhu, B. Liu, C. Wang, R. Ma, *J. Mater. Chem. A* **2019**, 7, 5353.
- [20] B. Roose, J.-P. C. Baena, K. C. Gödel, M. Graetzel, A. Hagfeldt, U. Steiner, A. Abate, *Nano Energy* **2016**, 30, 517.
- [21] A. Farooq, I. M. Hossain, S. Moghadamzadeh, J. A. Schwenzer, T. Abzieher, B. S. Richards, E. Klampaftis, U. W. Paetzold, *ACS Appl. Mater. Interfaces* **2018**, 10, 21985.
- [22] X. Li, J. Yang, Q. Jiang, H. Lai, S. Li, J. Xin, W. Chu, J. Hou, *ACS Nano* **2018**, 12, 5605.
- [23] B. Roose, C. M. Johansen, K. Dupraz, T. Jaouen, P. Aebi, U. Steiner, A. Abate, *J. Mater. Chem. A* **2018**, 6, 1850.
- [24] J. Wei, F. Guo, X. Wang, K. Xu, M. Lei, Y. Liang, Y. Zhao, D. Xu, *Adv. Mater.* **2018**, 30, e1805153.
- [25] J. Chen, H. Dong, L. Zhang, J. Li, F. Jia, B. Jiao, J. Xu, X. Hou, J. Liu, Z. Wu, *J. Mater. Chem. A* **2020**, 131, 6050.
- [26] P. Wang, R. Li, B. Chen, F. Hou, J. Zhang, Y. Zhao, X. Zhang, *Adv. Mater.* **2020**, 32, 1905766.
- [27] Z. Hawash, L. K. Ono, Y. Qi, *Adv. Mater. Interfaces* **2018**, 5, 1700623.
- [28] Z. Hawash, L. K. Ono, S. R. Raga, M. V. Lee, Y. Qi, *Chem. Mater.* **2015**, 27, 562.
- [29] G. Divitini, S. Sacovich, F. Matteocci, L. Cinà, A. Di Carlo, C. Ducati, *Nat. Energy* **2016**, 1, 1.
- [30] Q. Dong, Y. Shi, C. Zhang, Y. Wu, L. Wang, *Nano Energy* **2017**, 40, 336.
- [31] Q. Jiang, X. Zhang, J. You, *Small* **2018**, 14, 1801154.
- [32] M. Park, J.-Y. Kim, H. J. Son, C.-H. Lee, S. S. Jang, M. J. Ko, *Nano Energy* **2016**, 26, 208.
- [33] L. Xiong, M. Qin, G. Yang, Y. Guo, H. Lei, Q. Liu, W. Ke, H. Tao, P. Qin, S. Li, H. Yu, G. Fang, *J. Mater. Chem. A* **2016**, 4, 8374.
- [34] G. Yang, H. Lei, H. Tao, X. Zheng, J. Ma, Q. Liu, W. Ke, Z. Chen, L. Xiong, P. Qin, Z. Chen, M. Qin, X. Lu, Y. Yan, G. Fang, *Small* **2017**, 13, 1601769.
- [35] Y. Bai, Y. Fang, Y. Deng, Q. Wang, J. Zhao, X. Zheng, Y. Zhang, J. Huang, *ChemSusChem* **2016**, 9, 2686.
- [36] X. Ren, D. Yang, Z. Yang, J. Feng, X. Zhu, J. Niu, Y. Liu, W. Zhao, S. F. Liu, *ACS applied materials & interfaces* **2017**, 9, 2421.
- [37] Q. Jiang, L. Zhang, H. Wang, X. Yang, J. Meng, H. Liu, Z. Yin, J. Wu, X. Zhang, J. You, *Nat Energy* **2017**, 2, 6050.
- [38] U. Thakur, U. Kwon, M. M. Hasan, W. Yin, D. Kim, N. Y. Ha, S. Lee, T. K. Ahn, H. J. Park, *Sci. Rep.* **2016**, 6, 35994.
- [39] E. Avigad, L. Etgar, *ACS Energy Lett.* **2018**, 3, 2240.
- [40] J. Wu, X.-Y. Guo, Z.-Y. Xie, *Chin. Phys. Lett.* **2012**, 29, 98801.
- [41] D. Angmo, X. Peng, A. Seeber, C. Zuo, M. Gao, Q. Hou, J. Yuan, Q. Zhang, Y.-B. Cheng, D. Vak, *Small* **2019**, 15, e1904422.
- [42] J. Yang, Z. Yuan, X. Liu, S. Braun, Y. Li, J. Tang, F. Gao, C. Duan, M. Fahlman, Q. Bao, *ACS Appl. Mater. Interfaces* **2018**, 10, 16225.
- [43] D. Angmo, X. Peng, J. Cheng, M. Gao, N. Rolston, K. Sears, C. Zuo, J. Subbiah, S.-S. Kim, H. Weerasinghe, R. H. Dauskardt, D. Vak, *ACS Appl. Mater. Interfaces* **2018**, 10, 22143.
- [44] Z. Shariatnia, *Renewable Sustainable Energy Rev.* **2020**, 119, 109608.
- [45] J. Troughton, K. Hooper, T. M. Watson, *Nano Energy* **2017**, 39, 60.
- [46] M. Li, Y.-M. Xie, X. Xu, Y. Huo, S.-W. Tsang, Q.-D. Yang, Y. Cheng, *Org. Electron.* **2018**, 63, 159.
- [47] Y. Galagan, F. Di Giacomo, H. Gorter, G. Kirchner, I. de Vries, R. Andriessen, P. Groen, *Adv. Energy Mater.* **2018**, 8, 1801935.
- [48] K. Hwang, Y.-S. Jung, Y.-J. Heo, F. H. Scholes, S. E. Watkins, J. Subbiah, D. J. Jones, D.-Y. Kim, D. Vak, *Adv. Mater.* **2015**, 27, 1241.
- [49] C. Besleaga, L. E. Abramiuc, V. Stancu, A. G. Tomulescu, M. Sima, L. Trinca, N. Plugaru, L. Pintilie, G. A. Nemnes, M. Iliescu, H. G. Svavarsson, A. Manolescu, I. Pintilie, *J. Phys. Chem. Lett.* **2016**, 7, 5168.
- [50] J. Bisquert, E. J. Juarez-Perez, *J. Phys. Chem. Lett.* **2019**, 10, 5889.
- [51] J. A. McLeod, L. Liu, *J. Phys. Chem. Lett.* **2018**, 9, 2411.
- [52] A. Ciccio, A. Latini, *J. Phys. Chem. Lett.* **2018**, 9, 3756.
- [53] I. Deretzis, E. Smecca, G. Mannino, A. La Magna, T. Miyasaka, A. Alberti, *J. Phys. Chem. Lett.* **2018**, 9, 3000.
- [54] S.-W. Lee, S. Kim, S. Bae, K. Cho, T. Chung, L. E. Mundt, S. Lee, S. Park, H. Park, M. C. Schubert, S. W. Glunz, Y. Ko, J. Yun, Y. Kang, H.-S. Lee, D. Kim, *Sci. Rep.* **2016**, 6, 38150.
- [55] D. Wei, T. Wang, J. Ji, M. Li, P. Cui, Y. Li, G. Li, J. M. Mbengue, D. Song, *J. Mater. Chem. A* **2016**, 4, 1991.
- [56] L. Meng, J. You, Y. Yang, *Nat. Commun.* **2018**, 9, 5265.
- [57] F. T. F. O'Mahony, Y. H. Lee, C. Jellott, S. Dmitrov, D. T. J. Bryant, J. R. Durrant, B. C. O'Regan, M. Graetzel, M. K. Nazeeruddin, S. A. Haque, *J. Mater. Chem. A* **2015**, 3, 7219.
- [58] Y. Ouyang, Y. Li, P. Zhu, Q. Li, Y. Gao, J. Tong, L. Shi, Q. Zhou, C. Ling, Q. Chen, Z. Deng, H. Tan, W. Deng, J. Wang, *J. Mater. Chem. A* **2019**, 7, 2275.
- [59] Y. Ouyang, L. Shi, Q. Li, J. Wang, *Small Methods* **2019**, 3, 1900154.
- [60] F. Verbakel, S. C. J. Meskers, R. A. J. Janssen, *Appl. Phys. Lett.* **2006**, 89, 102103.
- [61] J. Kong, S. Song, M. Yoo, G. Y. Lee, O. Kwon, J. K. Park, H. Back, G. Kim, S. H. Lee, H. Suh, K. Lee, *Nat. Commun.* **2014**, 5, 5688.
- [62] G. Abdelmageed, L. Jewell, K. Hellier, L. Seymour, B. Luo, F. Bridges, J. Z. Zhang, S. Carter, *Appl. Phys. Lett.* **2016**, 109, 233905.

- [63] N. Aristidou, C. Eames, I. Sanchez-Molina, X. Bu, J. Kosco, M. S. Islam, S. A. Haque, *Nat. Commun.* **2017**, *8*, 15218.
- [64] N. Aristidou, I. Sanchez-Molina, T. Chotchuangchutchaval, M. Brown, L. Martinez, T. Rath, S. A. Haque, *Angew. Chem., Int. Ed. Engl.* **2015**, *54*, 8208.
- [65] T. Supasai, N. Rujisamphan, K. Ullrich, A. Chemseddine, T. Dittrich, *Appl. Phys. Lett.* **2013**, *103*, 183906.
- [66] Y. C. Kim, N. J. Jeon, J. H. Noh, W. S. Yang, J. Seo, J. S. Yun, A. Ho-Baillie, S. Huang, M. A. Green, J. Seidel, T. K. Ahn, S. I. Seok, *Adv. Energy Mater.* **2016**, *6*, 1502104.
- [67] Q. Chen, H. Zhou, T.-B. Song, S. Luo, Z. Hong, H.-S. Duan, L. Dou, Y. Liu, Y. Yang, *Nano Lett.* **2014**, *14*, 4158.
- [68] S. Tang, Y. Deng, X. Zheng, Y. Bai, Y. Fang, Q. Dong, H. Wei, J. Huang, *Adv. Energy Mater.* **2017**, *7*, 1700302.